

## Combinatorial methods in advanced battery materials design

Eric McCalla<sup>1\*</sup>, Matthew Parmaklis<sup>1†</sup>, Sarish Rehman<sup>1†</sup>, Ethan Anderson<sup>1†</sup>, Shipeng Jia<sup>1†</sup>,  
Alex Hebert<sup>1†</sup>, Karlie Potts<sup>1†</sup>, Antranik Jonderian<sup>1†</sup>, Tham Adhikari<sup>1,2†</sup>, and Michel Adamic<sup>1†</sup>.

<sup>1</sup>Department of Chemistry, McGill University, Montreal, H3A 0B8, Canada

<sup>2</sup>Now at: Department of chemistry, 80 St. George St, Toronto.

† Contributed equally

\* Corresponding author: [eric.mccalla@mcgill.ca](mailto:eric.mccalla@mcgill.ca)

**Abstract:** In the search for better performing battery materials, researchers have increasingly ventured into more and more complex composition spaces, including numerous pseudo-quaternary materials, with numerous substitutions into those materials being either explored experimentally or proposed based on computation. Given the vast composition spaces that need to be explored, experimental combinatorial science can play an important role in accelerating the development of advanced battery materials and is arguably the best means to obtain a sufficiently large data set to truly bring a high degree of precision to advanced computational techniques such as machine-learning. Herein, we present a robust high-throughput synthesis platform that is currently being used in the McCalla lab at McGill University to study Li-ion cathodes, anodes and solid electrolytes, as well as Na-ion cathodes. The synthesis methods used are presented in detail, as are the high-throughput characterization techniques we utilize regularly (X-ray diffraction, electrochemical testing and electrochemical impedance spectroscopy). We quantitatively determine the high precision and reproducibility achieved by this combinatorial system and also demonstrate its versatility by presenting for the first time combinatorial data for two high-power anodes for Li-ion batteries ( $\text{TiNb}_2\text{O}_7$  and  $\text{W}_3\text{Nb}_{14}\text{O}_{44}$ ) as well as solid state electrolyte

$\text{Li}_7\text{La}_3\text{Zr}_2\text{O}_{12}$ . Our methods reproduce accurately the results from the literature for bulk samples, indicating that the high-throughput methodology utilizing small mg-scale samples scale up extremely well to the larger sample sizes typically used in both the literature and industry. The throughput of this combinatorial infrastructure has a current limit of 896 XRD patterns and 896 EIS patterns a week, and 448 cyclic voltammograms running simultaneously.

## 1. Motivation

Over the past two decades, there has been a dramatic increase in the amount of energy storage required due to the current push toward the widespread use of electric vehicles and the effort to develop storage systems capable of supporting a large amount of intermittent renewable energies on the grid. This has resulted in a dramatic increase in the amount of research performed in advanced battery materials and has yielded a vast array of compositions of high interest for future research. Figure 1 shows a list of some of the material families of current interest in advanced battery materials research. Each of the cathode, anode and electrolyte have resulted in solid state chemistry looking at the impact of a wide variety of substitutions into base structures which are already pseudo-binaries or ternaries. These studies, relying solely on researchers' intuition, have resulted in great strides in the performance of all 3 components. Nonetheless, progress has been limited by the rate at which researchers can make and characterize advanced battery materials. At the same time, computational groups have accelerated development by performing calculations on many possible substitutions and this has resulted in an extremely long list of possible materials that need to be vetted experimentally. This is illustrated dramatically by a paper looking at substitutions into  $\text{Li}_7\text{La}_3\text{Zr}_2\text{O}_{12}$  (a garnet solid state electrolyte and a strong candidate for next-generation all-solid batteries).[1]The computational study predicted that 61 different elements could be substituted into the structure, and only a handful have been tested experimentally as single

substitutions with fewer still looking at co-substitution.[1] Given that computations performed to predict some key properties (e.g. ionic conductivity) are very time consuming (especially when 61 different substitutions are deemed viable) and computations also struggle to account for regions of solid solution (given the large supercells required when low levels of substitution are performed), there is a strong need for an accelerated experimental screening of all key components in advanced batteries.

Herein, we present a versatile high-throughput infrastructure that can synthesize and characterize a wide variety of solid materials of high interest for batteries research. This platform has been developed at McGill university in the McCalla lab since 2018 when the lab started. The list of materials currently being studied by these methods include all materials listed in Figure 1, such that the current focus of the group is to develop advanced high energy Li-ion batteries, Na-ion batteries, all-solid batteries, and high-power Li-ion batteries. Of note, the high-throughput X-ray diffractometer uses Mo-radiation, permitting a more rapid collection of the data, and it will be demonstrated here that despite the rapid collection time a very high quality data set is obtained that can be quantified to obtain both accurate lattice parameters and phase compositions. The other important methods for screening battery materials (electrochemical testing and impedance spectroscopy) will also be presented in detail, with a focus on 3 classes of materials we have not published elsewhere, demonstrating how adaptable this infrastructure is to various structures and compositions. The typical workflow illustrating the rate of data collection is shown in Figure 2.

## **2. Methodology and representative results:**

### **2.1 Synthesis**

Two synthesis routes are readily used in our combinatorial studies: co-precipitation and sol-gel. Both begin by mixing various volumes of precursor solutions, as illustrated in Figure 2a. To date,

we have successfully performed such syntheses with the following reactant elements: Li, Na, Ni, Mn, Co, Al, Ti, Zr, La, Nb, W, and we are currently expanding the repertoire vastly in order to perform systematic substitution studies wherein 63 different substituents can be tested simultaneously. Of those listed above, only Ti could not be prepared as an aqueous solution. The precursors must not only be soluble, but the bi-products formed with the counter-ions must also decompose readily during the synthesis such that nitrates and acetates are particularly appealing for high-throughput studies. The total volumes dispensed vary from 25 to 250  $\mu\text{L}$  (the lower volumes allow dispensing onto an alumina plate as described in refs. [2–6] while the larger volumes must be dispensed into small cups and yield enough product to make dense pellets needed for solid electrolyte studies). The next step in the co-precipitation reaction route is to add a precipitator such as ammonia or ammonium bicarbonate. Then, after drying, the samples can be heated up in a tube or box furnace up to high temperatures to yield the products of interest. This method is used exclusively in the group to study cathodes for Li-ion batteries as this synthesis route is the only one used commercially. We have reported on this numerous times.[2–6]

For all other classes of materials and for substitution studies, the sol-gel route has proven to be far more adaptable. For example, attempting to use titanium in a co-precipitation synthesis results in a titanium precipitate that floats thereby preventing intimate mixing with the other cations that form a precipitate that settles to the bottom of the container. To date, sol-gel has been successfully adapted for all syntheses we have attempted on the combinatorial scale, including some that use titanium [8]. Following the combination of the precursor solutions, citric acid is added and the samples are then dried overnight (either at 70  $^{\circ}\text{C}$ , and/or at 200  $^{\circ}\text{C}$  under vacuum). Figure 3 shows samples at various steps in this synthesis, including the drying when a smokestack is required to prevent neighboring samples from popping during citrate burn-off and mixing with each other.

This smokestack is normally kept in place for the next step in the synthesis: heating to  $>500\text{ }^{\circ}\text{C}$  in air to completely eliminate the bi-products formed during the sol-gel process. The smokestack is then removed. For electrode materials the samples are then heated to their synthesis temperatures (800-1050  $^{\circ}\text{C}$  have been utilized so far in either air or flowing oxygen). For solid electrolytes, the samples are first pressed into pellets using an in-house-designed high-throughput die set (each sample is pressed between two cylinders made from hardened 440C stainless steel). Though each sample must be pressed on its own to avoid differences in pressure between thicker and thinner pellets, the process takes about an hour and permits 64 quality pellets to be formed at a pressure of 1.0 GPa. Finally, high-temperature sintering/synthesis is performed at temperatures as high as 1250  $^{\circ}\text{C}$ . This yields samples with relative densities as high as 95 % [7].

## **2.2 X-ray diffraction**

Powder X-ray diffraction patterns of the as prepared samples are collected on a combinatorial X-ray diffractometer (combi-XRD) devoted to this research program. The instrument, a Panalytical Empyrean diffractometer, uses Mo  $K\alpha$  radiation and operates in the transmission mode with a GaliPIX area detector. The use of Mo radiation has a number of advantages for combinatorial work: (1) the absorption is much lower than Cu radiation such that transmission is possible, thereby utilizing scattering from the entire sample, (2) the wavelength is less than half that of Cu so that a smaller angle range is required to obtain the same information, we use 4-30 $^{\circ}$ , instead of 10-70 $^{\circ}$  that would be needed for Cu radiation, (3) the splitting between the  $K\alpha_1$  and  $K\alpha_2$  peaks is more severe, such that two sharp peaks are readily obtained at nearly all angles instead of one broad peak as seen in Cu radiation scans (the consequence of this splitting will be discussed further later on, but it significantly improves the precision such that any expected loss in precision due to the smaller wavelength is negated). Figure 4 shows representative XRD spectra collected on this

combi-XRD system, in all case the scans are about 10 minutes long and the counts in the strongest peaks are greater than 1000 which is considered a decent benchmark for scans to be of a high enough quality to perform meaningful Rietveld refinement despite the samples being as small as 2 mg. Another critical feature of the combi-XRD patterns is that the background is remarkably low. This is attributed to the fact that Mo radiation causes no fluorescence with the 3d transition metals that are most often utilized in battery materials, whereas these same cations fluoresce strongly with Cu radiation. This will of course be the reverse situation where one uses materials with cations near Mo in the periodic table. Nonetheless, to date this combi-XRD system has proven to yield a very low, flat background as demonstrated in all XRD patterns included herein. This means that any amorphous products would be detected quite readily, where a Cu-radiation XRD systems might not resolve them so easily.

The fact that the background is so low also means that this system is remarkably sensitive to minority phases and is therefore ideal for mapping phase diagrams where co-existing phases occur in the majority of samples. To illustrate this, we use an example from our recent report on Li-La-Ti-O phase diagram. A particular sample showed a 5 wt. %  $\text{TiO}_2$  phase with a majority perovskite phase, quantified using Rietveld refinement. The largest  $\text{TiO}_2$  peak in that sample had a height of 170 counts above the background of 55 counts such that the noise in the background is only 7.4 (square roots of the counts). Thus, the 5 %  $\text{TiO}_2$  peak was 23 times larger than the noise, indicating that even 1 %  $\text{TiO}_2$  would be about 5 times above the noise and certainly detectable in that particular case, and this is again using data collected in 10 min on approximately 10 mg of sample.[7]

These advantages of using a Mo-radiation system for combi-XRD of course come with some concerns that must be considered here. The first concern is that the lower wavelength results in a

reduced precision in q-space (scattering vector) and as such could be expected to give a lower resolution during refinement, thereby yielding a large uncertainty in the extracted lattice parameters. Table 1 compares lattice parameters from this study with those obtained from the literature with Cu radiation, along with their uncertainties when reported. Systematically, the uncertainty on the lattice parameters obtained herein is comparable to that from the literature, showing that the Mo radiation does not result in a reduced precision in lattice parameters, and we attribute this to the large splitting of  $K\alpha_1$  and  $K\alpha_2$  peaks giving two distinct sharp peaks to fit as shown in Figure 4, rather than the broad peak often obtained with Cu radiation wherein the two peaks overlap. So in q-space the peaks being fit have very comparable widths.

Furthermore, figure 4 (and the rest of the XRD figures in this article) shows that excellent quality fits are obtained with this data. For the purpose of this article, LeBail fits are used throughout with the program Rietica. Table 2 shows the results for the quality parameters ( $R_P$  and  $R_{WP}$ ) for these fits. Often times, researchers use a threshold of about 10% to determine whether a fit is high quality or not; it is important to recognize that this threshold depends on the type of radiation used. Table 2 shows R values of 12-19% obtained with the combi-XRD, whereas 2-3% was obtained on an instrument using Cu radiation. However, the Cu pattern had a far higher background (6.5% of the height of the strongest peak), table 2 shows that when a flat background is added to the Mo pattern to make it 6.5 % of the largest peak and fitting is repeated, then the R values are 1-2 % and are in fact slightly smaller than those obtained with Cu radiation. We therefore need a new threshold for quality fits for our combi-XRD and estimate based on the present study that values for  $R_P$  in the range 15-20% are indicative of excellent quality fits.

Another important concern regarding the use of Mo radiation is that the large splitting of the two peaks may mask secondary phases if their peaks are present near the  $K\alpha_2$  peaks of the primary

phase. The technique we use to detect secondary phases is to first subtract the  $K\alpha_2$  signal and for ease of comparison with the rest of the literature we then convert to the scattering angles that would be obtained with Cu  $K\alpha_1$  radiation. The product of this process is shown for the P2 sample in the lower panel of figure 4. The subtraction of  $K\alpha_2$  is consistently very effective giving very small fluctuations where the  $K\alpha_2$  peaks were present before processing. This implies that the detection of secondary phases can be done quite easily with a very high sensitivity as discussed later. Table 1 also shows that the lattice parameters extracted by fitting this corrected pattern match those obtained from fitting the original pattern very closely. Due to the relative ease of visually identifying phases from these corrected patterns, we use these extensively in high-throughput studies and will discuss these converted patterns for the rest of this article. Figure 5 shows 3 patterns in the Li[Ni,Mn,Co]O<sub>2</sub> composition spaces wherein the top pattern shows a single phase while the other two patterns show secondary phases appearing at the most unfortunate position of being at the  $K\alpha_2$  peak positions of the primary phase. The top panel shows the smallest oscillation indicated by the red arrows, such that this indicates our limitation in detection of secondary phases in the unlikely cases such as this. However, even in such an unfortunate case, figure 5 clearly shows the high sensitivity to secondary phases. In fact, to date, phase compositions as low as 1% by weight have been detected and quantified with Rietveld refinement.[7]

The final concern that needs to be addressed regarding the combi-XRD is, in fact, a question of the reproducibility of the synthesis. Given the small amount of samples, small contaminations can yield large fluctuations in the results. Figure 6 shows sets of triplicates (*i.e.* each pattern is an overlap of 3 different samples: red, blue and black) for samples made in the Na-Fe-Mn-O pseudo-ternary system. These triplicates were synthesized on 3 different combinatorial sample sets and, in fact, the 3 triplicates were located at different positions on each plate. Of the 30 patterns shown,

we see 2 outliers, while the others show excellent reproducibility. This is representative, in fact the complete set of triplicates for this experiment was 108 samples (36 sets) and showed only 6 outliers. It should also be mentioned that in all cases, the occasional outliers show the same peaks as the others, but in different ratios implying that there is a fluctuation in the ratios of phases present in a multi-phase region, rather than an actual difference in the phases obtained. Comparable triplicate sets have been obtained for all systems studied to date once the synthesis is optimized (this reproducibility screening has proven to be a very useful and necessary step in the optimization of the synthesis and poor reproducibility of XRD triplicates was the motivation for the use of the smokestack described above).

To date, the high-throughput synthesis/XRD has been successfully utilized to make materials in the following systems, all of which reproduce closely results from the literature on bulk samples: Li-Ni-Co-Mn-O, Na-Fe-Mn-O, Li-La-Ti-O, Li-La-Zr-O, W-Nb-O, and Ti-Nb-O. This shows the remarkable versatility of the combinatorial infrastructure and demonstrates the wide window of materials studies now available for further study. The next two sections focus on the high-throughput methods used to determine battery performance once quality materials are confirmed from XRD.

### **2.3 Electrochemical screening**

Figure 6(f-g) shows some of the steps/hardware needed to perform electrochemical screening in high-throughput. This methodology has been described in detail elsewhere.[2] In essence, this results in 64 small electrodes on pads of a printing circuit board. The copper pads have been covered with aluminum foil in order to prevent reaction during electrochemical cycling. This method has resulted in precision/reproducibility of <1% in average discharge voltages and 6-7% in specific capacity for both Li-ion and Na-ion cathodes.[2,8] This implies that the screening of

energy density (product of voltage and capacity) is at the 6-7% level as well. In both cases, the results were found to be highly consistent with samples made in bulk as reported in the literature, thereby ensuring good scale-up from the mg-scale of the combinatorial work up to the g- and kg-scale of interest in industrial settings. This high-throughput electrochemical testing has also been used to screen extended cycling (on the order of 10 cycles) and thus provides moderate detail into the extended cycling of the cathode materials. This has been demonstrated for both Li-ion cathodes [2] and Na-ion cathodes [9].

Although we have established this method for cathodes and vetted the reproducibility and accuracy thoroughly, here we demonstrate the feasibility of using this 64-sample cell for rate testing of high power Li-ion anodes for the first time. This involves our verifying that useful information about rate performance can be obtained from the high-throughput measurements and that the synthesis can be adapted to these new materials. Of highest concern, the high-throughput measurements can only be performed as cyclic voltammograms (all 64 samples have a common counter electrode so they all have the same voltage). Although rate performance can be tested in both CV and the more traditional galvanostatic cycling, the results will differ (the two methods only give the same capacities at very slow rates). To do this test, we first focus on  $\text{TiNb}_2\text{O}_7$  as it is well studied in the literature [10,11].

Figure 8 shows both the XRD pattern and the electrochemistry obtained on a combinatorial sample of  $\text{TiNb}_2\text{O}_7$ . The combi-XRD pattern is consistent with results from the literature for bulk samples and table 1 shows that the lattice parameters match very closely.[10] Our synthesis of the combinatorial samples involved heating to 1000 °C. The CV shown for  $\text{TiNb}_2\text{O}_4$  is in excellent agreement with that published in the literature.[11] The peak potentials we obtain here are 1.57 and 1.72 V for charge and discharge respectively at 0.1 V/h; while those from the literature are

1.59 and 1.68 at 0.36 V/h from ref. [10]. This indicates very little overpotential resulting from either the quality of the combinatorial sample or the use of the combinatorial cell. The rate performance was further studied here by increasing the voltage sweep rate. The resulting CVs are shown in the inset to figure 8 while the specific capacities are included in table 3. The CVs show a large overpotential at the highest sweep rate, demonstrating that we are near the limit of what the material can do in terms of rate performance, it should also be noted that the currents at the highest sweep rate are very near to the limit of what the potentiostat can supply, such that 2 V/h is hereby established as the maximum sweep rate that can be used in our combinatorial setup. In order to compare to the literature, we recognize that nearly all the capacity in the CV is obtained for a 1 V window (1-2 V), such that a sweep at 1 V/h is roughly equivalent to galvanostatic cycling at 1 C (1 h charge, 1 h discharge). Similarly, we compare the fastest cycling (2 V/h) to the 2 C galvanostatic cycling from the literature. Table 3 shows that the capacities obtained here are very close to those obtained from the literature for rate testing at comparable time windows via galvanostatic methods in ref. [9]. This establishes the high-throughput electrochemistry as a viable method to determine the rate performance for high power anodes.

There are 3 classes of materials garnering a lot of attention as high power anodes:  $\text{Li}_4\text{Ti}_5\text{O}_{12}$ , Ti-Nb-O materials with various stoichiometries, and W-Nb-O materials with various stoichiometries. All 3 are of interest for further study by combinatorial means as substitutions impact their performances significantly. Here, we demonstrate the viability of making W-Nb-O materials on the combinatorial scale. W-Nb-O materials have recently gathered a lot of interest. [13,14]. Recently  $\text{W}_3\text{Nb}_{14}\text{O}_{44}$  was synthesized at 1000 °C as nanorods and showed promising electrochemistry.[13] Figure 9 shows XRD and electrochemistry results obtained for a combinatorial sample of  $\text{W}_3\text{Nb}_{14}\text{O}_{44}$  synthesized at 1000 °C. It is of high interest that despite the

modest temperatures used, the XRD pattern shows a near pure-phase material consistent with the literature as confirmed with the lattice parameters in table 1. Furthermore, this material shows highly competitive capacities of 215 mAh/g at the slow cycling rate of 0.1V/h, quite competitive with the values obtained for the materials published in ref. [14]. It is also of interest that the rate performance for this material is quite a bit inferior to that of  $\text{TiNb}_2\text{O}_7$ , as shown in table 3 and is in remarkable agreement with galvanostatic results for the nanorods synthesized in ref. [14]. This success is further confirmation that the high-throughput electrochemistry will screen rate performance in a manner that scales-up well to non-combinatorial approaches. This also demonstrates that although the rate performance in CV mode is different from that obtained from galvanostatic, we still obtain good discrimination between the rate performance of different materials, such that this will prove to be an effective means to screen the rate performance of anodes.

Based on the success in reproducing results for  $\text{TiNb}_2\text{O}_7$  and the fact that combinatorial synthesis of  $\text{W}_3\text{Nb}_{14}\text{O}_{44}$  was successful, it is clear that the high-throughput methods established herein will be suitable for the study of a wide variety of high-power anode compositions, and we are currently studying the entire Ti-W-Nb-O pseudo-ternary system using the sol-gel synthesis route that we demonstrate here for the first time for high-power anodes.

## **2.4 Electrochemical impedance spectroscopy**

For solid electrolytes, pellets must first be made as described in the synthesis section. Figure 6(c) shows the 64 pellets after gold coating with a homemade mask, while (d-e) show the cell design used to apply pressure to all 64 pellets during electrochemical impedance spectroscopy (EIS) measurements. The high-throughput EIS system was assembled in-house using a 64-channel multiplexer and a BioLogic potentiostat operated with a house-written code. This system can be

utilized to determine the ionic conductivity of the solid electrolytes and readily yields values for both bulk and grain boundary conductivities, key properties to be studied in order to develop quality solid electrolytes.

The first system studied with this combinatorial EIS system was the Li-La-Ti-O system in which perovskite materials have garnered a lot of attention as potential solid electrolytes. The details of this study are presented elsewhere [7], but it is important to recognize that with the high-throughput infrastructure described here we were able to make high density pellets (95%) with conductivities comparable to those obtained in bulk studies ( $>10^{-3}$  S cm<sup>-1</sup> for bulk conductivities and total conductivities as high as  $5.0 \times 10^{-5}$  S cm<sup>-1</sup>). Figure 10 shows a typical high-throughput impedance spectrum from a Li-La-Ti-O material with high conductivity along with the result of an automated fit used to extract conductivities. The figure shows an excellent quality fit both in the low frequency region shown in the main panel, and the high-frequency region in the inset. Such high quality spectra and data fitting serve as the proof of concept that high precision studies of solid electrolytes can be performed using the high-throughput infrastructure discussed herein. Of note, repeats of 8 of samples made in air with conductivities of about  $5.0 \times 10^{-5}$  S/cm gave standard deviations of  $0.4\text{-}0.7 \times 10^{-5}$  S/cm (i.e. 8-14 %). It is important to keep in mind that researchers are often looking for order of magnitude gains in conductivity such that a high-throughput system operating at the 10-15% precision range will be a powerful screening tool.

There are a very wide variety of promising materials of interest as potential solid electrolytes and the impact of substitutions into these materials is now a pressing interest. We demonstrate here that the high-throughput synthesis route developed herein can also be used to prepare Li-La-Zr-O garnet materials that continue to be of high interest for solid batteries. Figure 11 shows the XRD pattern along with the fit used to extract lattice parameters. Table 1 shows again excellent

agreement between the lattice parameters obtained for this small combinatorial sample (10 mg) and the literature values obtained from bulk syntheses. Now that the synthesis is established, we are performing a thorough study of the pseudo-ternary Li-La-Zr-O system as well as a systematic substitution study looking at the impact of a very wide variety of substitutions into the garnet shown in Figure 11.

## **Conclusions**

A combinatorial work-flow has been established in the McCalla lab at McGill University wherein 896 XRD patterns can be collected per week, with the potential to collect the same number of EIS spectra, and 448 electrode materials can be cycled simultaneously. The synthesis methods used to make the hundreds of samples weekly rely on either co-precipitation or sol-gel synthesis routes, both of which have been optimized for high-throughput methods (64 samples made at once). Herein, we demonstrate not only the speed but also the precision and reproducibility of the high-throughput synthesis as illustrated by the XRD patterns. The high-throughput XRD utilizes Mo radiation in a transmission mode. The XRD patterns are shown to yield lattice parameters with the same precision as a typical Cu radiation instrument, while detecting secondary phases at levels as low as 1 wt. %. The high-throughput electrochemistry on these combinatorial samples, having been demonstrated as a reliable and reproducible method elsewhere, was shown to be viable for rate performance testing of high-power anodes for the first time. Finally, the precision and reliability of high-throughput EIS was demonstrated, such that screening of solid electrolytes is now realistic. We demonstrate the synthesis of Li-La-Zr-O garnet solid electrolytes in high-throughput for the first time. This article therefore establishes this infrastructure for the screening of all key components in advanced batteries: cathodes (Li-ion and Na-ion), anodes and solid

electrolytes. Importantly, all high-throughput measurements are shown to be sensitive enough to give good discrimination at levels needed to effectively screen next-generation battery materials.

## Acknowledgements

This work was funded by the Natural Sciences and Engineering Research Council of Canada under the auspices of a Discovery grant as well as an FRQNT new researcher grant and the New Frontier's Research Fund. Much of the infrastructure described and utilized herein was obtained thanks to the Canadian Foundation for Innovation.

## References

- [1] L. J. Miara, W. D. Richards, Y. E. Wang, and G. Ceder, *First-Principles Studies on Cation Dopants and Electrolyte|Cathode Interphases for Lithium Garnets*, Chem. Mater. **27**, 4040 (2015).
- [2] K. P. Potts, E. Grignon, and E. McCalla, *Accelerated Screening of High-Energy Lithium-Ion Battery Cathodes*, ACS Appl. Energy Mater. **2**, 8388 (2019).
- [3] E. McCalla, A. W. Rowe, R. Shunmugasundaram, and J. R. Dahn, *Structural Study of the Li–Mn–Ni Oxide Pseudoternary System of Interest for Positive Electrodes of Li-Ion Batteries*, Chem. Mater. **25**, 989 (2013).
- [4] E. McCalla, G. H. Carey, and J. R. Dahn, *Lithium Loss Mechanisms during Synthesis of Layered  $\text{Li}_x\text{Ni}_2 - \text{XO}_2$  for Lithium Ion Batteries*, Solid State Ion. **219**, 11 (2012).
- [5] E. McCalla, C. M. Lowartz, C. R. Brown, and J. R. Dahn, *Formation of Layered–Layered Composites in the Li–Co–Mn Oxide Pseudoternary System during Slow Cooling*, Chem. Mater. **25**, 912 (2013).
- [6] C. R. Brown, E. McCalla, C. Watson, and J. R. Dahn, *Combinatorial Study of the Li–Ni–Mn–Co Oxide Pseudoquaternary System for Use in Li–Ion Battery Materials Research*, ACS Comb. Sci. **17**, 381 (2015).
- [7] E. McCalla, *STRUCTURAL AND ELECTROCHEMICAL STUDIES OF THE LI-MN-NI-O AND LI-CO-MN-O PSEUDO-TERNARY SYSTEMS*, (2013).
- [8] A. Jonderian and E. McCalla, *Stabilization of Metastable Li-La-Ti-O Perovskite Materials with in-Situ Sintering Additives*, Chem. Mater. **Submitted**, (2020).
- [9] T. Adhikari, A. Hebert, M. Adamič, J. Yao, K. Potts, and E. McCalla, *Development of High-Throughput Methods for Sodium-Ion Battery Cathodes*, ACS Comb. Sci. **22**, 311 (2020).
- [10] J.-T. Han, Y.-H. Huang, and J. B. Goodenough, *New Anode Framework for Rechargeable Lithium Batteries*, Chem. Mater. **23**, 2027 (2011).

- [11] V. Aravindan, J. Sundaramurthy, A. Jain, P. S. Kumar, W. C. Ling, S. Ramakrishna, M. P. Srinivasan, and S. Madhavi, *Unveiling  $TiNb_2O_7$  as an Insertion Anode for Lithium Ion Capacitors with High Energy and Power Density*, *ChemSusChem* **7**, 1858 (2014).
- [12] R. Inada, R. Kumasaka, S. Inabe, T. Tojo, and Y. Sakurai,  *$Li^+$  Insertion/Extraction Properties for  $TiNb_2O_7$  Single Particle Characterized by a Particle-Current Collector Integrated Microelectrode*, *J. Electrochem. Soc.* **166**, A5157 (2019).
- [13] K. J. Griffith, K. M. Wiaderek, G. Cibin, L. E. Marbella, and C. P. Grey, *Niobium Tungsten Oxides for High-Rate Lithium-Ion Energy Storage*, *Nature* **559**, 556 (2018).
- [14] L. Yan, J. Shu, C. Li, X. Cheng, H. Zhu, H. Yu, C. Zhang, Y. Zheng, Y. Xie, and Z. Guo,  *$W_3Nb_{14}O_{44}$  Nanowires: Ultrastable Lithium Storage Anode Materials for Advanced Rechargeable Batteries*, *Energy Storage Mater.* **16**, 535 (2019).
- [15] J. Awaka, N. Kijima, H. Hayakawa, and J. Akimoto, *Synthesis and Structure Analysis of Tetragonal  $Li_7La_3Zr_2O_{12}$  with the Garnet-Related Type Structure*, *J. Solid State Chem.* **182**, 2046 (2009).
- [16] A. Jonderian and E. McCalla, *The Role of Metal Substitutions in the Development of Li Batteries, Part II: Solid Electrolytes*, *Mater. Adv.* **Accepted**, (2021).
- [17] A. Hebert and E. McCalla, *The Role of Metal Substitutions in the Development of Li Batteries, Part I: Cathodes*, *Mater. Adv.* **Submitted**, (2021).
- [18] P. Roy and S. K. Srivastava, *Nanostructured Anode Materials for Lithium Ion Batteries*, *J. Mater. Chem. A* **3**, 2454 (2015).

## **Tables:**

**Table 1:** Lattice parameters obtained herein from Le Bail fits with uncertainties in brackets, along with corresponding values from the literature.

Material	$a$ (Å)	$b$ (Å)	$c$ (Å)	$\beta$ (°)	Source
Na <sub>2/3</sub> Fe <sub>0.5</sub> Mn <sub>0.5</sub> O <sub>2</sub>	2.918(1)		11.303(1)		this study, raw*
Na <sub>2/3</sub> Fe <sub>0.5</sub> Mn <sub>0.5</sub> O <sub>2</sub>	2.919(1)		11.305(1)		this study, converted*
LiCoO <sub>2</sub>	2.817(1)		14.066(2)		this study
LiCoO <sub>2</sub>	2.8185		14.0664		COD: 1550397
TiNb <sub>2</sub> O <sub>7</sub>	20.3660(9)	3.7944(2)	11.9130(7)	120.435(4)	this study
TiNb <sub>2</sub> O <sub>7</sub>	20.3908(4)	3.8039(2)	11.9171(6)	120.313(8)	ref. [11]
W <sub>3</sub> Nb <sub>14</sub> O <sub>44</sub>	20.986(1)		3.818(1)		this study
W <sub>3</sub> Nb <sub>14</sub> O <sub>44</sub>	21.02		3.824		ref. [13]
Li <sub>7</sub> La <sub>3</sub> Zr <sub>2</sub> O <sub>12</sub>	13.114(1)		12.685(1)		This study
Li <sub>7</sub> La <sub>3</sub> Zr <sub>2</sub> O <sub>12</sub>	13.134(4)		12.663(8)		ref. [14]

\* Both entries are extracted from the same data. The first line is the result of fitting the original data with Mo radiation ( $\lambda = 0.70926$  Å for  $K\alpha_1$ ,  $\lambda = 0.713543$  Å for  $K\alpha_2$ ), the second was obtained after subtracting the  $K\alpha_2$  peaks and converting to copper  $K\alpha_1$  angles ( $\lambda = 1.54051$  Å for  $K\alpha_1$ ). This later method is used throughout the rest of this article and the rest of this table.

**Table 2:** Quality parameters ( $R_P$ ,  $R_{WP}$ ) for the Le Bail fits of  $\text{Na}_{2/3}\text{Fe}_{0.5}\text{Mn}_{0.5}\text{O}_2$  materials obtained from both the high-throughput XRD utilizing Mo radiation and a standard laboratory XRD using Cu radiation. The background intensity column is the value of the background as a fraction of the maximum peak intensity. The full width at half maximum (FWHM) of two peaks is also included.

XRD type	$R_P$ (%)	$R_{WP}$ (%)	Background (%)	FWHM (@ $16^\circ$ )	FWHM (@ $66^\circ$ )
Cu radiation	3.05	3.16	6.5	0.11	0.41
Mo radiation	19.2	12.88	0.6	0.15**	0.42**
Mo radiation*	2.07	1.31	6.5	0.15**	0.42**

\* A background of 5.9 % of the largest peak intensity was added to all data points in the scan obtained with Mo radiation in order to yield a background comparable to that obtained in Cu-radiation X-ray diffractometers.

\*\* FWHM obtained after subtracting the  $K\alpha_2$  peak and converting to angles obtained for Cu  $K\alpha_1$  as described in the text.

**Table 3:** Rate performance of  $\text{TiNb}_2\text{O}_7$  and  $\text{W}_3\text{Nb}_{14}\text{O}_{44}$  tested in the combinatorial cell. All capacity values are specific discharge capacity.

Material	Specific discharge capacity (mAh/g)			
	Rate: 10 h/V	2.5 h/V	1 h/V	0.5 h/V
$\text{TiNb}_2\text{O}_7$	262	253	219	218
$\text{TiNb}_2\text{O}_7^*$		270 (2.7 h)	245 (1.2 h)	215 (0.55 h)
$\text{W}_3\text{Nb}_{14}\text{O}_{44}$	215	202	171	153
$\text{W}_3\text{Nb}_{14}\text{O}_{44}^*$	230 (4 h)	192 (2 h)	176 (1 h)	149 (0.5 h)

\* Capacities obtained from galvanostatic cycling and the indicated time for  $\frac{1}{2}$  cycles, extracted from refs. [11,14].

### **Figure captions:**

**Figure 1.** Illustrations of the motivation for experimental combinatorial screening of battery materials. Each of the key components (cathode, anode and electrolyte) in modern batteries and especially in next-generation batteries are complex compositions as highlighted here. In the diagram, the separator is soaked in a liquid electrolyte, while much current research is involved in substituting this with a solid electrolyte. The materials currently representing the state-of-the-art are all pseudo-binaries or ternaries with numerous substitutions having been proposed, studied and commercialized for each class of materials. These vast composition spaces cannot be studied in their entirety by any method, but combinatorial methods enable a far larger portion to be explored. The substituents lists are obtained from refs. [16,17] and the schematic of the battery was adapted from ref. [18].

**Figure 2.** Typical workflow of a combinatorial study utilized the infrastructure presented herein. The synthesis begins by dispensing mixtures of precursor solutions either with a solution-dispensing robot or by hand pipetting using precision micro-pipettes. After the synthesis described in the text, XRD is performed on all 64 samples using the combi-XRD with Mo-radiation (approximately 10 min per sample, for a total of 10 h). The samples utilized for XRD can then be assembled into an electrochemical cell to test their performance (electrodes) or their electrochemical stability (solid electrolytes). A separate batch of solid electrolytes needs to be synthesized and kept as pellets in order to perform conductivity measurements with impedance spectroscopy. In both cases, the results are correlated to the phase diagrams to obtain a map of the composition/structure/property relationships.

**Figure 3.** Images of the synthesis of Na-Fe-Mn-O materials: (a) samples after the drying step of the sol-gel synthesis showing the color gradients corresponding to composition, (b) the samples

are transferred to an alumina plate with an aluminum smokestack to prevent mixing during burn-off of the citrate bi-products, (c) the aluminum smokestack is removed prior to high-temperature synthesis, (d) the samples after transferring into the high-throughput XRD sample holder, all samples have a thin Mylar foil both below and above, (d) the samples in the combi-XRD operating in transmission mode.

**Figure 4.** XRD patterns of two layered oxides obtained in the combi-XRD: (a)  $\text{LiCoO}_2$ , (b)  $\text{Na}_{2/3}\text{Fe}_{1/2}\text{Mn}_{1/2}\text{O}_2$ , (c) the same pattern as obtained in (b) but with the  $\text{K}\alpha_2$  subtraction performed and the angle values converted to that which would have been obtained with copper radiation. All fits were obtained using the LeBail technique. In red are the  $R_p$  and  $R_{wp}$  values when a background of 341 is added to the data in order to match the typical background obtained with a Cu-radiation XRD.

**Figure 5.** Combi-XRD patterns of 3 materials in the Li-Ni-Mn-Co-O system after subtracting the Mo  $\text{K}\alpha_2$  peak and converting to angles obtained for Cu  $\text{K}\alpha_1$ . The topmost is single phase, while the other 2 are multi-phase with peaks that happen to lie at the same position as the  $\text{K}\alpha_2$  peaks of the unique phase in the topmost scan. The negligible peaks indicated by the yellow arrows in the topmost scan show that even in this worse-case-scenario, the combi-XRD system is capable of distinguishing phase co-existence from remnants of the  $\text{K}\alpha_2$  peaks.

**Figure 6.** A series of XRD patterns from the Na-Fe-Mn-O system. Each scan is an overlap of 3 different scans (red, blue and black) obtained from 3 different synthesis runs with the samples at different positions within the synthesis plates. Of the 30 scans shown, only 2 are outliers (note: the complete set was 108 scans, *i.e.* 36 triplicates, that contained 4 outliers only), highlighted by the two red boxes (in these boxes, 2 patterns match each other well, while the third shows some variation). This high level of reproducibility is typical for the combinatorial synthesis system.

**Figure 7.** Pictures of various steps required for electrochemical tests (cycling and EIS). Solid-state electrolyte samples at various stage of preparation for the high-throughput impedance measurements: (a) the samples are in-house designed high-throughput die-press, (b) 64 pellets after high-temperature synthesis, (c) gold coating of 64 pellets in our house-made masks, (d) 64 gold-coated pellets on the printed circuit board used for EIS measurements, (e) the top-plate of the cell used for EIS measurements with 64 spring mounted pistons that apply pressure to all pellets simultaneously. Steps in the cycling of electrode materials include (f) a printed circuit board with 64 electrodes prepared on it in order to perform cyclic voltammetry and (g) this same cell once assembled on the cycler.

**Figure 8.** Combinatorial XRD and electrochemical data obtained for a sample of  $\text{TiNb}_2\text{O}_7$  sample synthesized at 1050 °C. The lower panel shows the cycling curve calculated from the cyclic voltammogram obtained at 0.1 V/h. The inset shows the results of the rate testing, performed in order of increasing sweep rate. The study of the entire Ti-Nb-O pseudo-binary is underway.

**Figure 9.** Combinatorial XRD and electrochemical data obtained for a sample of  $\text{W}_3\text{Nb}_{14}\text{O}_{44}$  sample synthesized at 1050 °C. The lower panel shows the cycling curve calculated from the cyclic voltammogram obtained at 0.1 V/h. The inset shows the results of the rate testing, performed in order of increasing sweep rate. The study of the entire W-Nb-O pseudo-binary is underway and the secondary phase marked by \* is consistent with the phase diagram to be discussed in a later article.

**Figure 10.** Typical impedance spectroscopy spectrum obtained for perovskite solid electrolytes in the Li-La-Ti-O composition space. The combinatorial sample was about 20 mg large and fitting was performed in an automated batch mode along with the other 63 from the combinatorial set (all

of which are shown in Figure 2). The high quality fit is typical and yields high precision in the extracted conductivity values as discussed in the main text.

**Figure 11.** Combinatorial XRD pattern for a sample of  $\text{Li}_7\text{La}_3\text{Zr}_2\text{O}_{12}$  synthesized at 900 °C in air along with the result of a LeBail fit and the difference plot.

Figures:

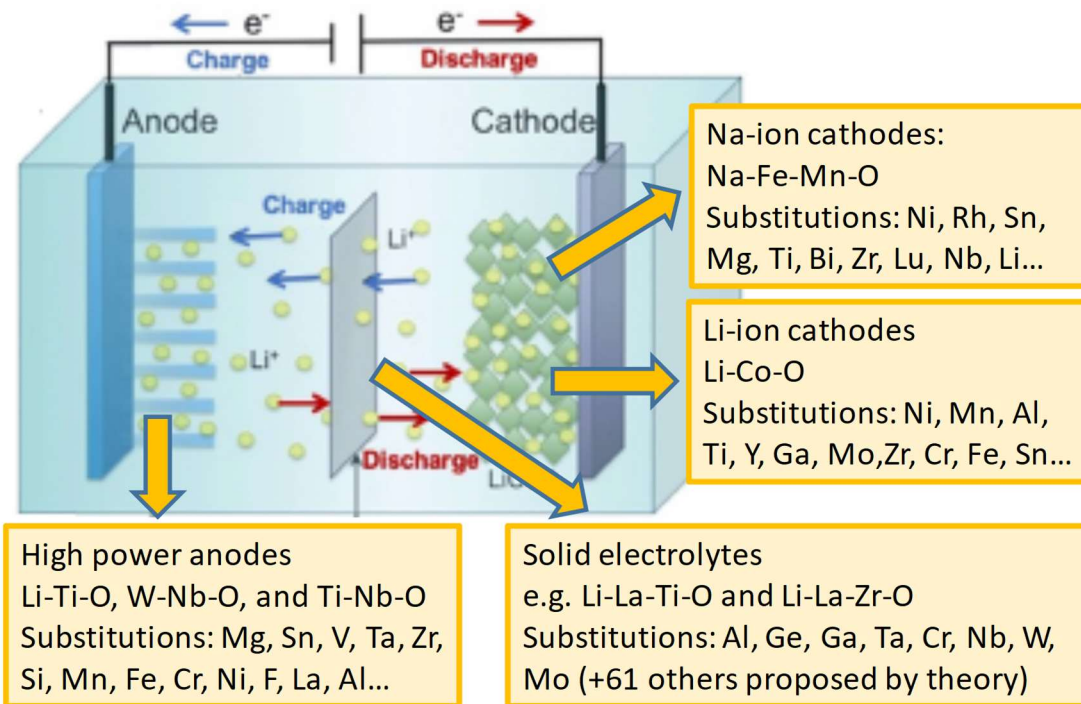


Figure 1.

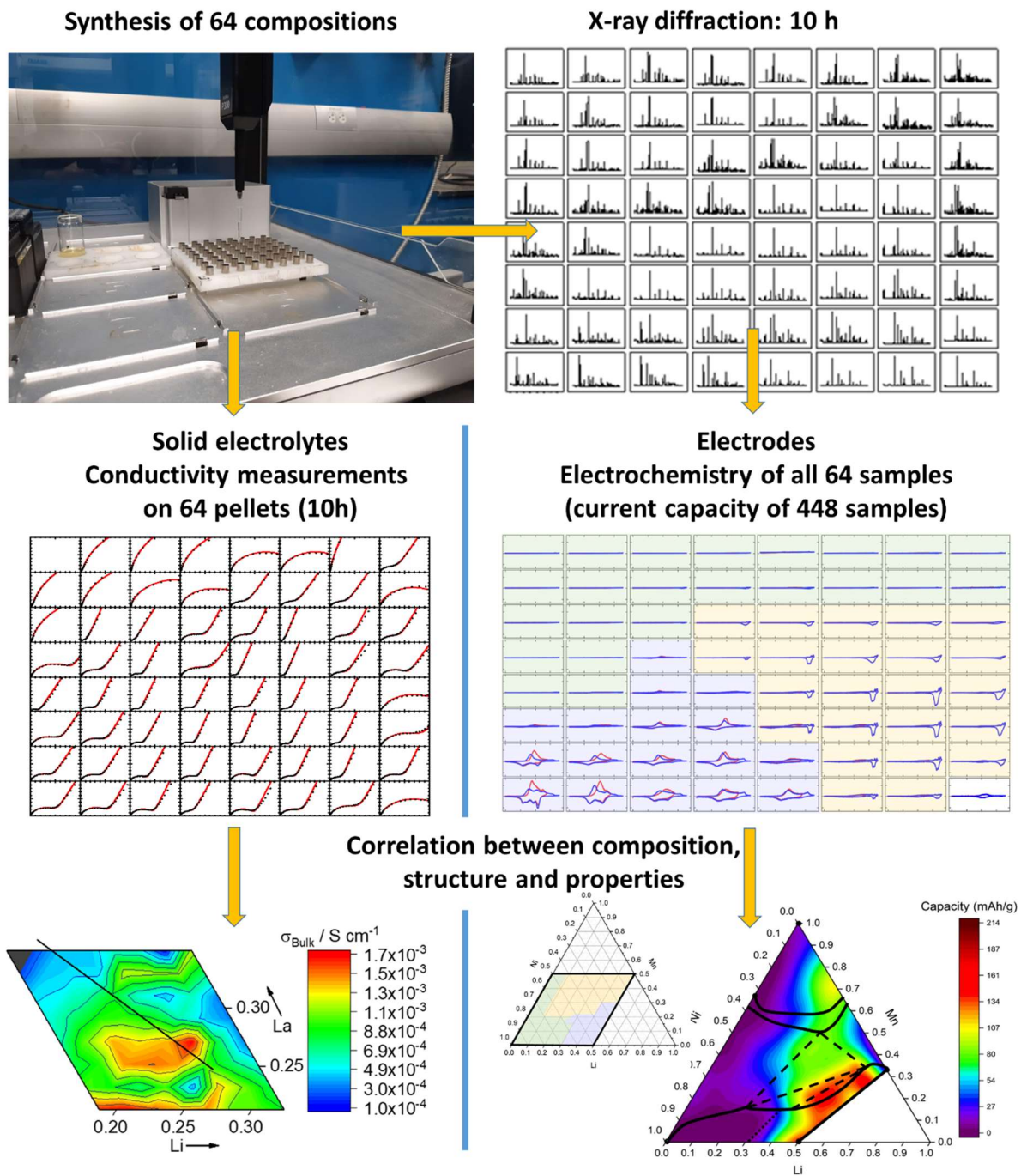


Figure 2.

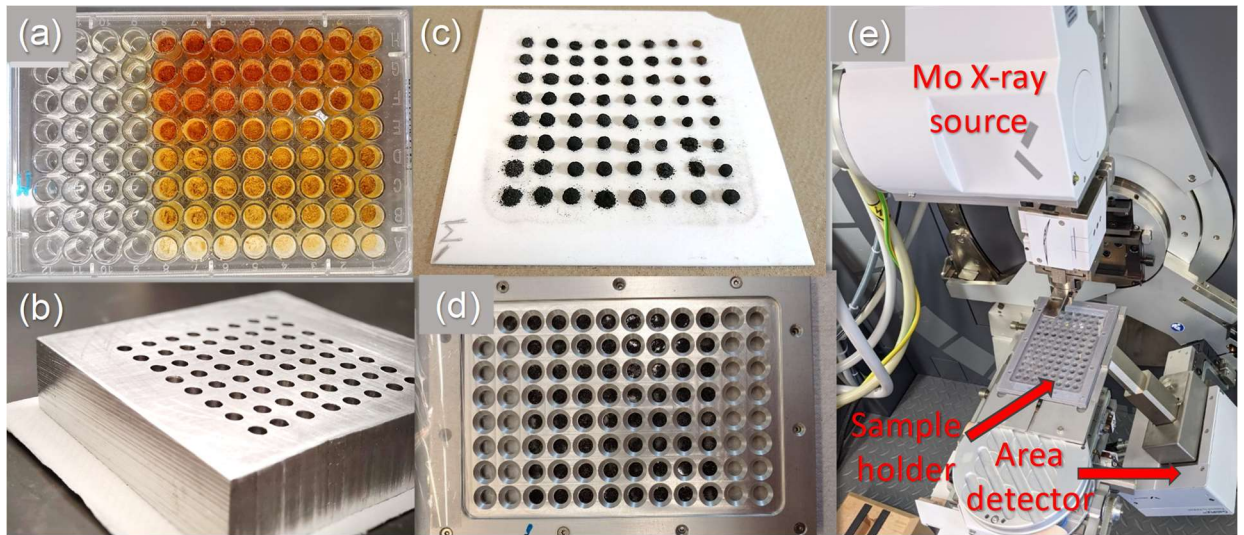


Figure 3.

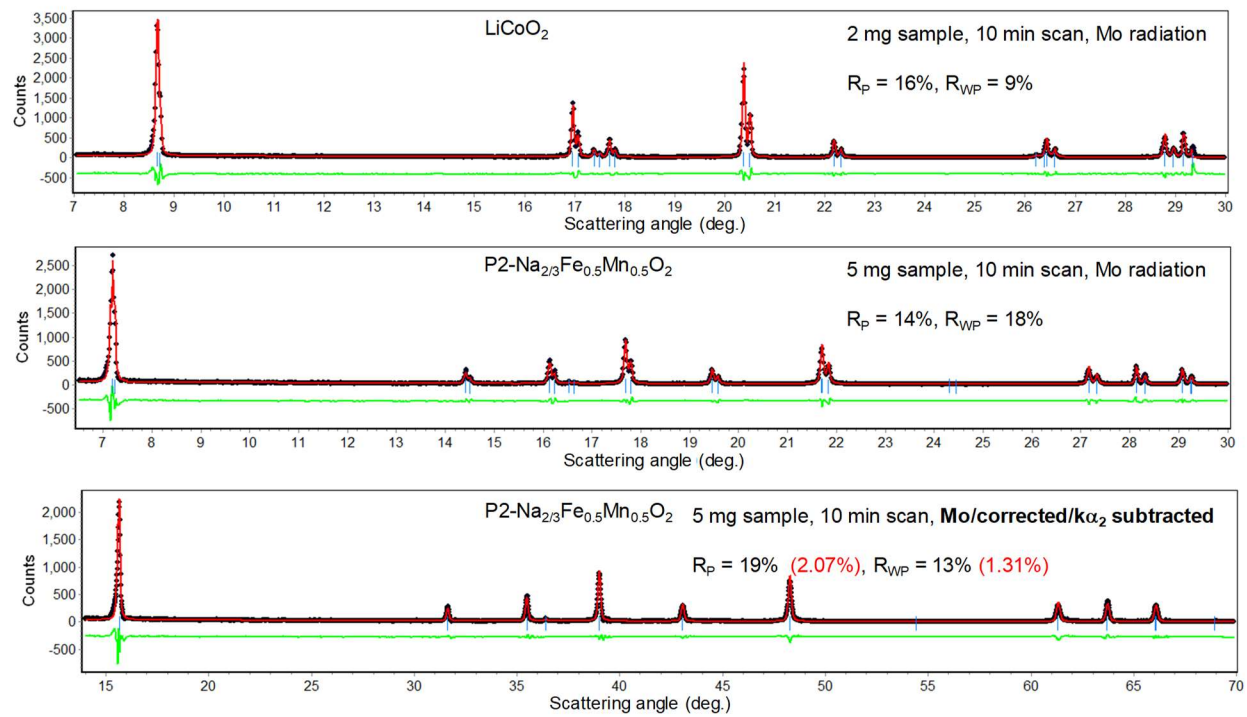


Figure 4.

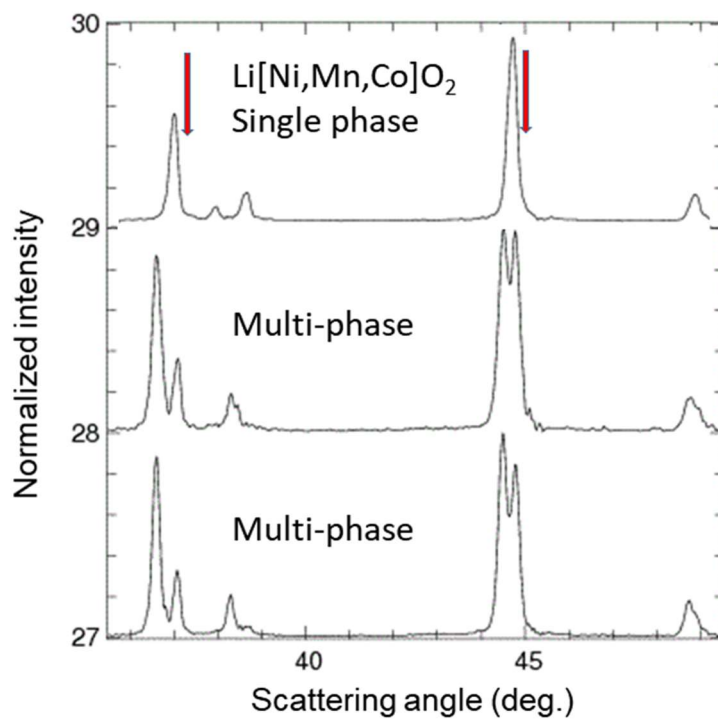
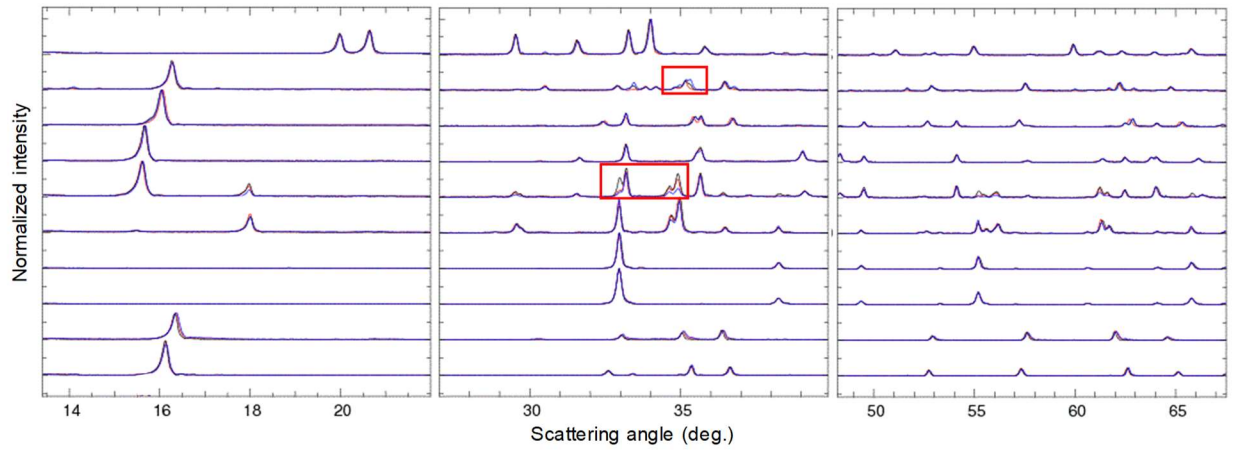
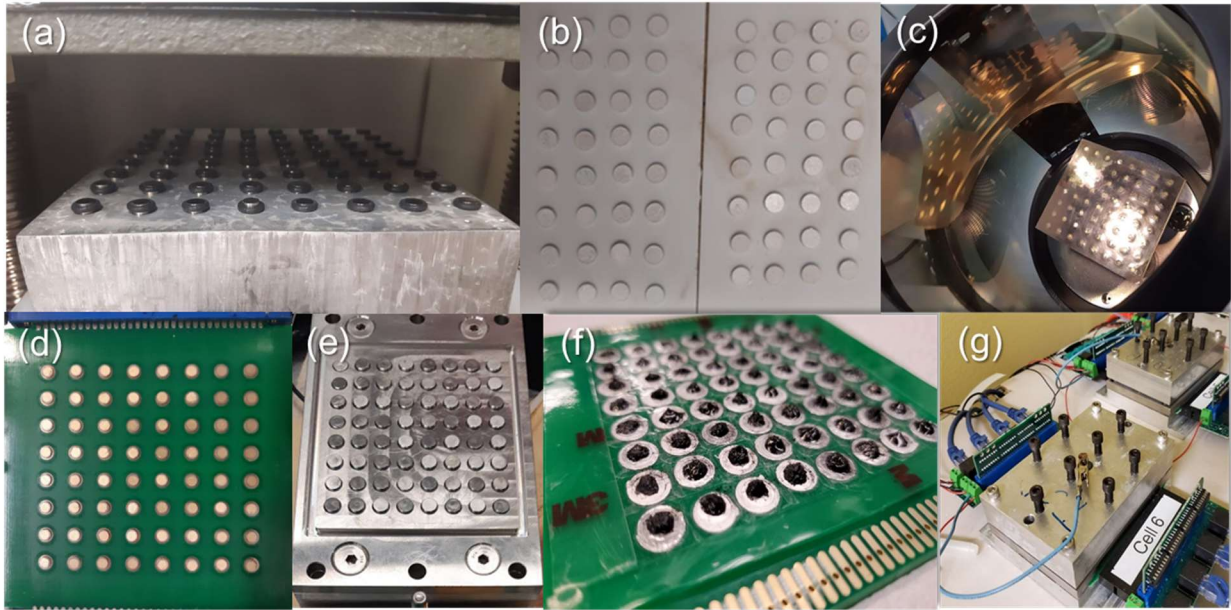


Figure 5.



**Figure 6.**



**Figure 7.**

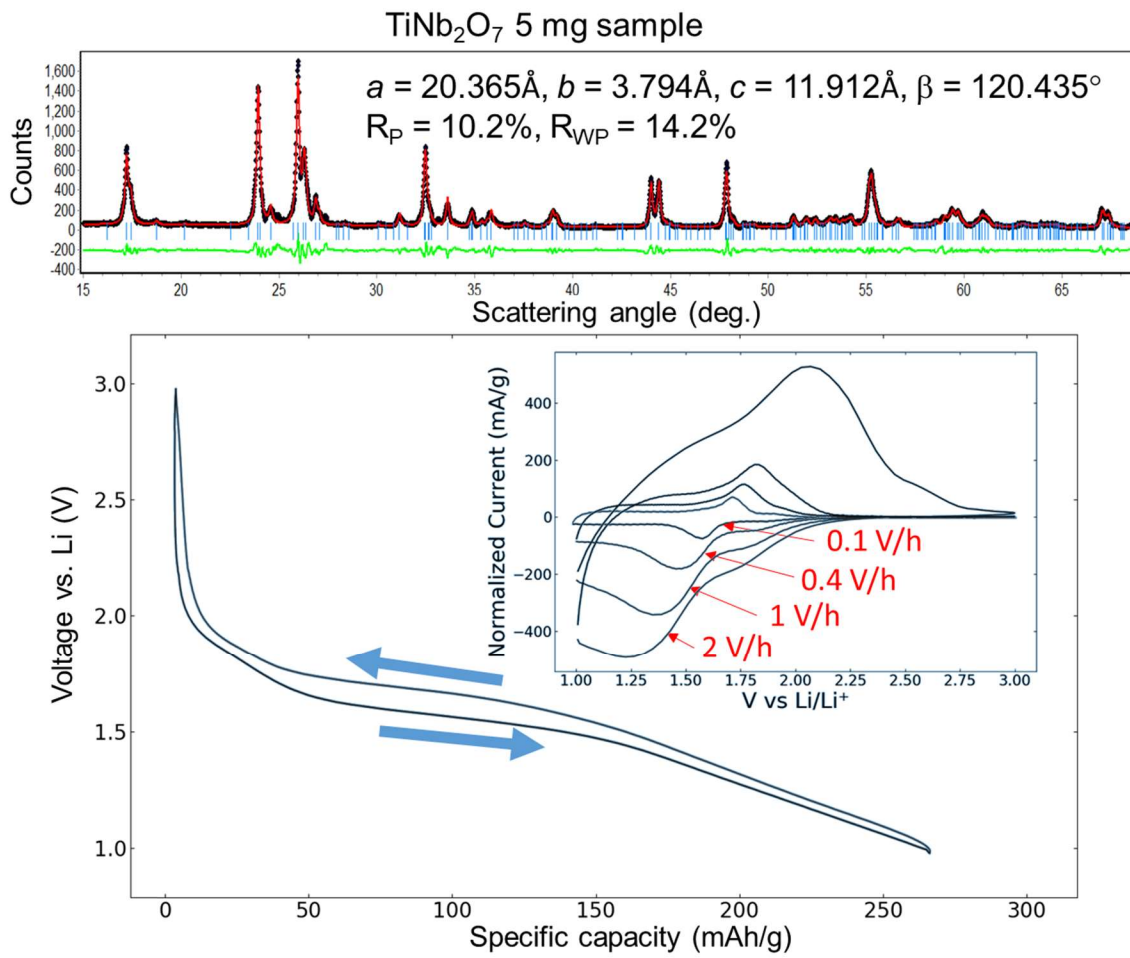


**Figure 8.**

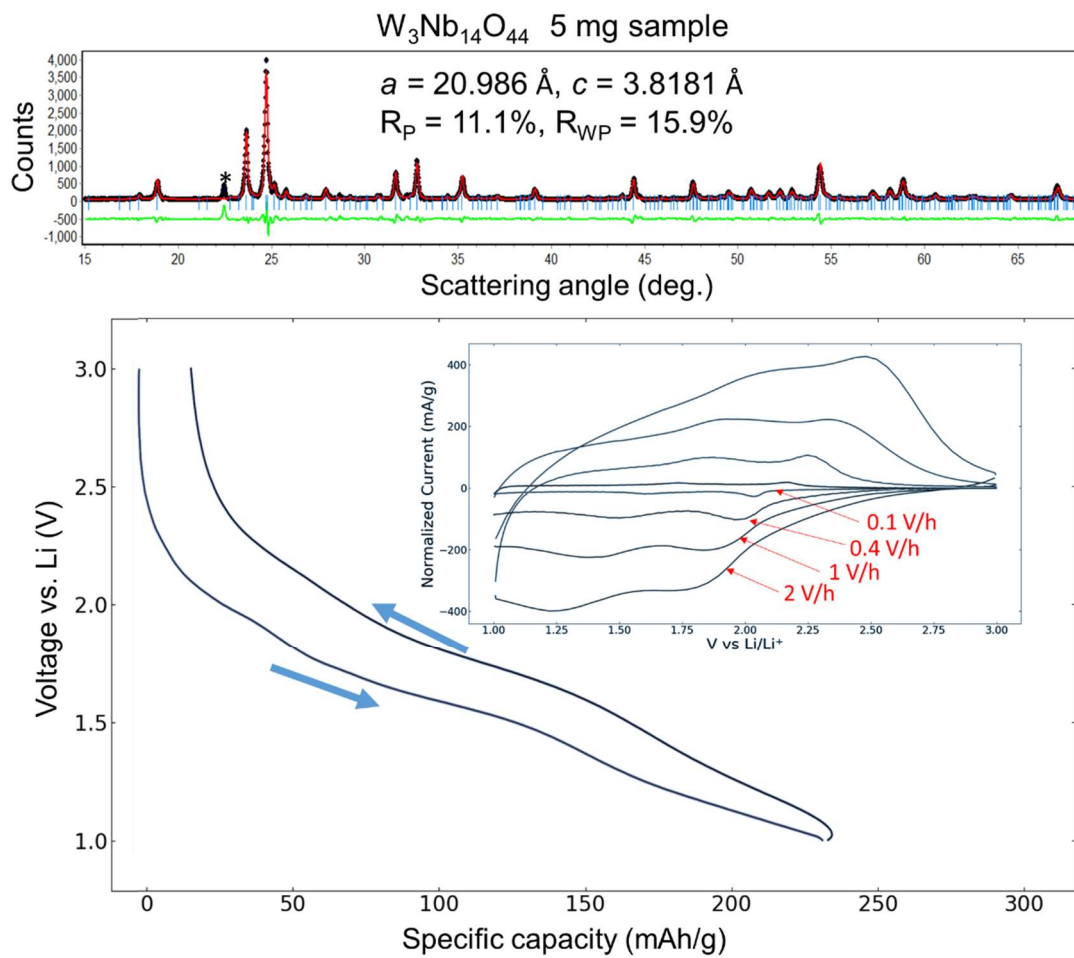


Figure 9.

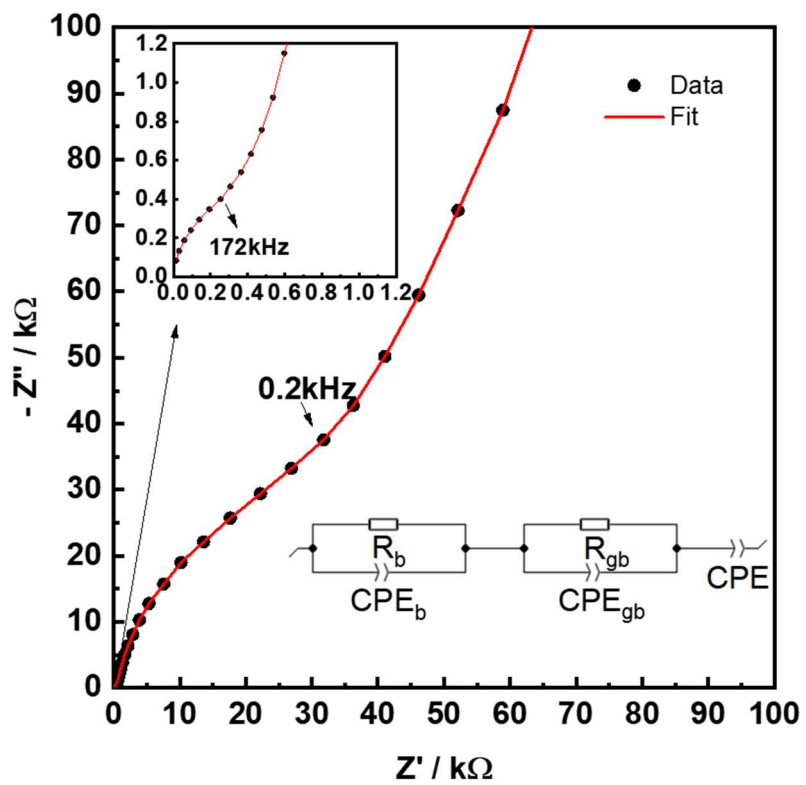


Figure 10.

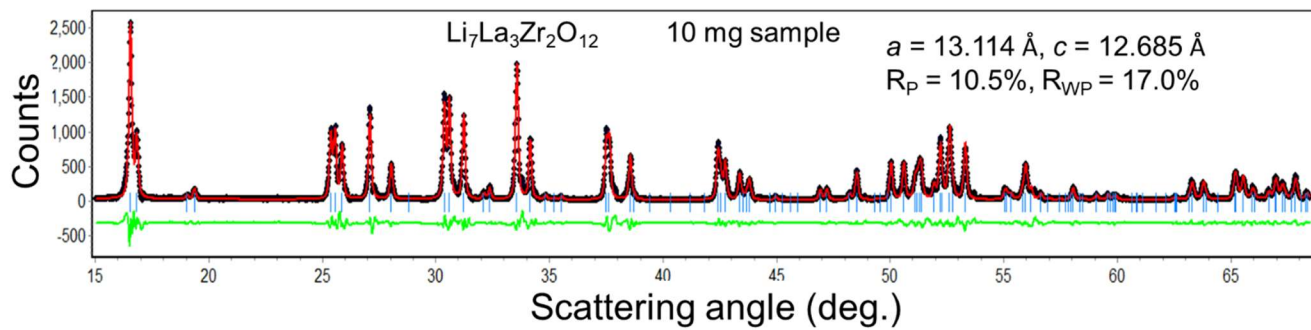


Figure 11.